Three-Phase Regenerative Converter with Controlled Flywheeling

SUBBANNA P. BHAT AND GOPAL K. DUBEY, SENIOR MEMBER, IEEE

Abstract—**The low-speed performance of a dc drive can be improved by operating the three-phase fully controlled bridge converter with controlled flywheeling. The analysis and performance of the drive with controlled flywheeling is described. The modes of operation of the converter system are identified, and a method of performance calculation, taking these modes of operation into account, is presented. Nomograms and the analytical method of calculating them are presented for the calculation of optimum value of filter inductance. The performance of the drive with controlled flywheeling is compared with that with conventional control. The modes of operation and certain aspects of drive performance are verified experimentally.**

I. INTRODUCTION

THREE-PHASE fully controlled converters are widely used in medium-power dc drives. The performance of such a drive in the converter output voltage range ($0.5 > E_{on} > -0.5$) can be improved by incorporating controlled flywheeling [1], [2]. In this paper, various aspects of three-phase converter system employing controlled flywheeling and feeding a separately excited dc motor are studied. The various modes of converter operation are identified, and their oscillograms are presented. The drive is analyzed using digital simulation, and various performance characteristics are obtained for a 2.2-kW motor. Nomograms are presented for the controlled flywheeling and the normal control techniques, from which a filter inductance can be calculated for any dc separately excited motor. The various parameters of the system performance with the controlled flywheeling are compared with those with the normal control technique for the same developed power. The modes of operation and certain aspects of the drive performance are verified experimentally.

II. MODES OF CONVERTER OPERATION

Fig. 1 shows the three-phase converter system and its equivalent circuit. Since the controlled flywheeling is possible only in a restricted range of the output voltage ($0.5 > E_{on} > -0.5$), the system operation is broadly classified into four modes of system operation which are listed in Table I.

In the case of dc motor load, if the armature current is discontinuous, the waveform of converter output voltage depends not only on the firing angle but also on the motor back

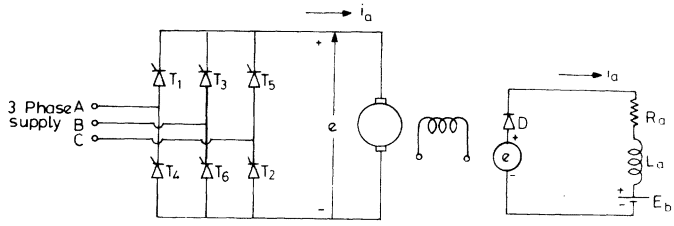

Fig. 1. Three-phase converter feeding dc motor. (a) Three-phase converter system. (b) Equivalent circuit.

TABLE I

Mode of System Operation	System Condition	Range of Firing Angle, α_p	Range of Flywheeling Angle, α_n
I	motoring	$0 < \alpha_p < \pi/3$	—
II	motoring	$\pi/3 < \alpha_p < 2\pi/3$	$\alpha_n = 0$
III	regeneration	$\alpha_p = (2\pi/3 - \delta)$	$0 < \alpha_n < \pi/3$
IV	regenerating	—	$\pi/3 < \alpha_n < 2\pi/3$

TABLE II

Mode of Converter Operation	System Condition[a]	Mode of System Operation	Nature of Armature Current[b]	Relationship Between α, β, *and* γ	Refer to Figure Number
1	M	I	D	$\alpha_p < \beta_p < \gamma_p$	2(a)
2	M	I	D	$\beta_p < \alpha_p < \gamma_p$	2(b)
3	M	I	D	$\beta_p < \gamma_p < \alpha_p$	2(c)
4	M	I	C	—	2(d)
5	M	II	D	$\beta_p < \pi/3 < \alpha_p$	2(e)
6	M	II	D	$\pi/3 < \beta_p < \alpha_p$	2(f)
7	M	II	C	—	2(g)
8	R	III	D	$\beta_n < \alpha_n < \gamma_n$	2(h)
9	R	III	C	—	2(i)
10	R	IV	D	$\beta_n < \alpha_n < \gamma_n$	2(j)
11	R	IV	D	$\beta_n < \gamma_n < \alpha_n$	2(k)
12	R	IV	C	—	2(l)

[a] M = motoring, R = regenerating.
[b] D = discontinuous, C = continuous.

EMF. In such cases, the actual waveshape depends upon the relative magnitudes of α_p, β_p, and γ_p (or α_n, β_n, and γ_n). Depending upon the waveshape of output voltage, the converter operation is classified into various modes which are listed in Table II and Fig. 2. A total of 12 modes are identified, among which modes 1–4 and 10–12 are common for both the controlled flywheeling and the normal control techniques. A brief description of all the modes is given as follows.

Four modes of continuous armature current exist (modes 4,

Paper IPCSD 85-01 and 83-29, approved by the Static Power Converter Committee of the IEEE Industry Applications Society for publication in this TRANSACTIONS. Manuscript released for publication January 21, 1985.

S. P. Bhat is with the Department of Electrical Engineering, Karnataka Regional Engineering College, P.O. Srinivasnagar-574 157, Dakshina Kannada District, Karnataka State, India.

G. K. Dubey was with the Department of Electrical Engineering, Virginia Polytechnic Institute, Blacksburg, VA 24061. He is now with the Department of Electrical Engineering, Indian Institute of Technology, Kanpur, 208016, India.

0093-9994/85/1100-1431$01.00 © 1985 IEEE

Authorized licensed use limited to: NATIONAL INSTITUTE OF TECHNOLOGY SURATHKAL. Downloaded on March 09,2021 at 06:21:29 UTC from IEEE Xplore. Restrictions apply.

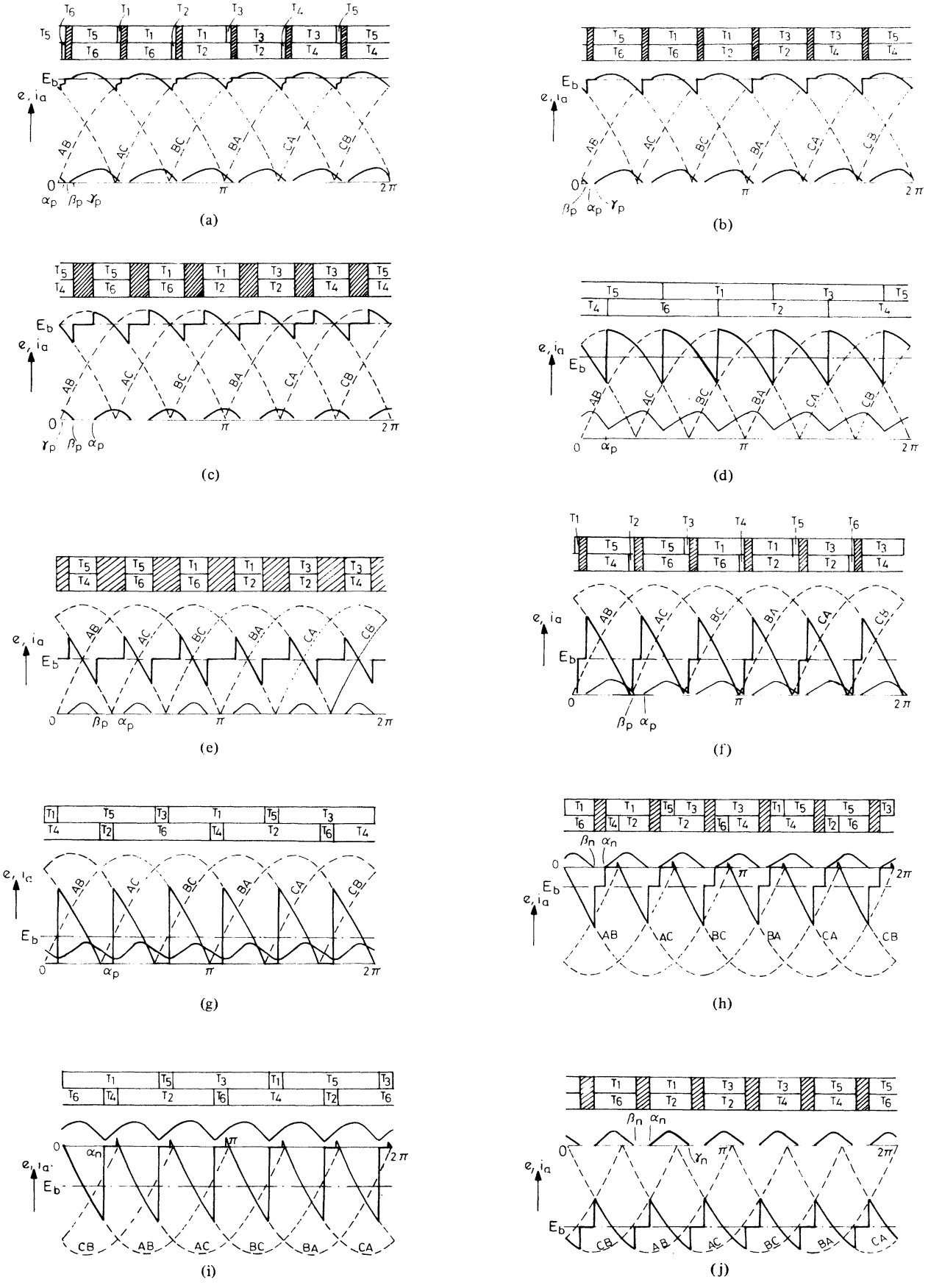

Fig. 2. Modes of converter operation. (a) Mode 1. (b) Mode 2. (c) Mode 3. (d) Mode 4. (e) Mode 5. (f) Mode 6. (g) Mode 7. (h) Mode 8. (i) Mode 9. (j) Mode 10. (k) Mode 11. (l) Mode 12.

Authorized licensed use limited to: NATIONAL INSTITUTE OF TECHNOLOGY SURATHKAL. Downloaded on March 09,2021 at 06:21:29 UTC from IEEE Xplore. Restrictions apply.

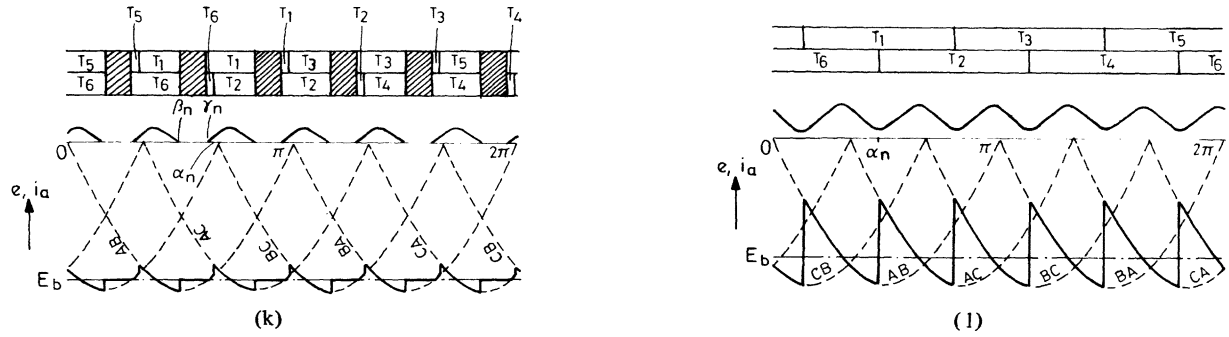

Fig. 2. (*Continued*).

7, 9, and 12), one for each of the four modes of system operation (Fig. 2(d), (g), (i), and (l)). In these modes, the conduction of incoming thyristors and the commutation of the already conducting thyristors occur simultaneously by virtue of line commutation.

In the case of mode 1 (Fig. 2(a)), when the thyristor T_1 is triggered at α_p, the armature current is nonzero, and therefore T_5 gets line commutated by T_1. (Symbols are defined in the Nomenclature at the end of the paper.) Since the instantaneous supply voltage is less than the motor back EMF, the armature current further reduces until it becomes zero. Since all the thyristors are supplied with the extended gate pulses, T_1 and T_6 regain conduction at γ_p, when the supply voltage becomes larger than the motor back EMF.

In the case of mode 2 (Fig. 2(b)), at the instant α_p the armature current has already become zero, and the supply voltage is smaller than the motor back EMF. Therefore, thyristors T_1 and T_6 come into conduction only at γ_p. Mode 3 (Fig. 2(c)) is different from the earlier modes in the sense that at the instant α_p, the supply voltage is larger than the motor back EMF. Therefore, the thyristors come into conduction as soon as they are triggered.

In the case of modes 1 and 3, a decrease in the motor back EMF converts these modes into mode 4, whereas in the case of mode 2, a decrease in the motor back EMF makes both β_p and γ_p approach the triggering instant α_p. Depending upon the magnitude of α_p, the decrease in motor back EMF would bring about the condition of either $\beta_p = \alpha_p < \gamma_p$ or $\beta_p < \alpha_p = \gamma_p$. In the former case, mode 2 converts itself to mode 1 and in the latter case to mode 3. Another remote possibility is that both β_p and γ_p would touch α_p simultaneously. In that case, mode 2 directly changes over to mode 4. A flowchart of the interrelationship of the various modes is given in Fig. 3. When mode 1 touches mode 4, the minimum of armature current occurs at $X = \gamma_p > \alpha_p$, and when mode 3 touches mode 4, at $X = \alpha_p > \gamma_p$. This information, which is useful for the calculation of maximum armature current ripple, is also noted in Fig. 3.

Modes 5–7 (Fig. 2(e)–(g)) belong to the second group (system operation mode II). In the case of modes 5 and 6, the armature current is discontinuous. In the case of mode 6, the output voltage becomes zero at $\pi/3$ (due to the flywheeling of the load) and remains so until β_p, whereas in the case of mode 5, the output voltage never becomes zero ($\beta_p < \pi/3$). However, if the motor back EMF is reduced, mode 5 becomes mode 6 and finally mode 7 (Fig. 3(b)). Note that mode 5 is

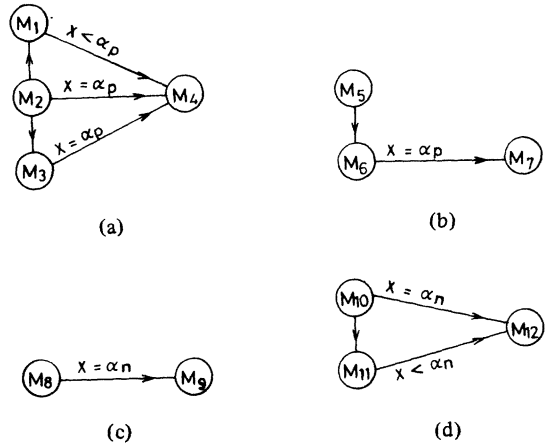

Fig. 3. Flowchart of converter operation. (a) System mode I. (b) System mode II. (c) System mode III. (d) System mode IV. Arrow indicates increase in I_a.

similar to mode 3, except that they belong to different modes of system operation.

Modes 8 and 9 (Fig. 2(h) and (i) and Fig. 3(c)) belong to the third group (system operation mode III). In this case, the system is under regeneration, and the flywheeling of the load occurs for certain duration.

Modes 10–12 (Fig. 2(j)–(l)) belong to the last group. There are two modes of discontinuous armature current (modes 10 and 11). In the case of mode 11, the armature current has become zero at β_n, but at γ_n, when the supply voltage becomes more positive than the generated EMF, the same set of thyristors (T_1 and T_6) regain conduction. At α_n, thyristor T_2 line commutates T_6. An increase in the generated EMF converts mode 11 to mode 12. In the case of mode 10 ($\alpha_n < \gamma_n$), if the generated EMF is increased, γ_n approaches α_n. Depending upon the magnitude of α_n, mode 10 may either become mode 11 or directly change over to mode 12. If mode 10 directly changes over to mode 12, the armature current assumes a minimum value at α_n. On the other hand, when mode 11 changes over to mode 12, it occurs at $X = \gamma_n < \alpha_n$. A flowchart of the modes belonging to this group is given in Fig. 3(d).

Note that all the modes described may not occur in a practical circuit, since some of them would require the armature circuit time constant to be very small. Oscillograms of nine out of 12 modes (except modes 1, 2, and 11), which are observed for a 2.2-kW motor (Table III) load, are recorded in Fig. 4.

Authorized licensed use limited to: NATIONAL INSTITUTE OF TECHNOLOGY SURATHKAL. Downloaded on March 09,2021 at 06:21:29 UTC from IEEE Xplore. Restrictions apply.

TABLE III
DC MOTOR SPECIFICATIONS

Output power	2.2 kW
Armature voltage	220 V
Shunt field excitation	220 V
Current rating	11.6 A
Rated speed	1500 r/min
Armature resistance	2.0 Ω
Armature inductance	32.5 mH

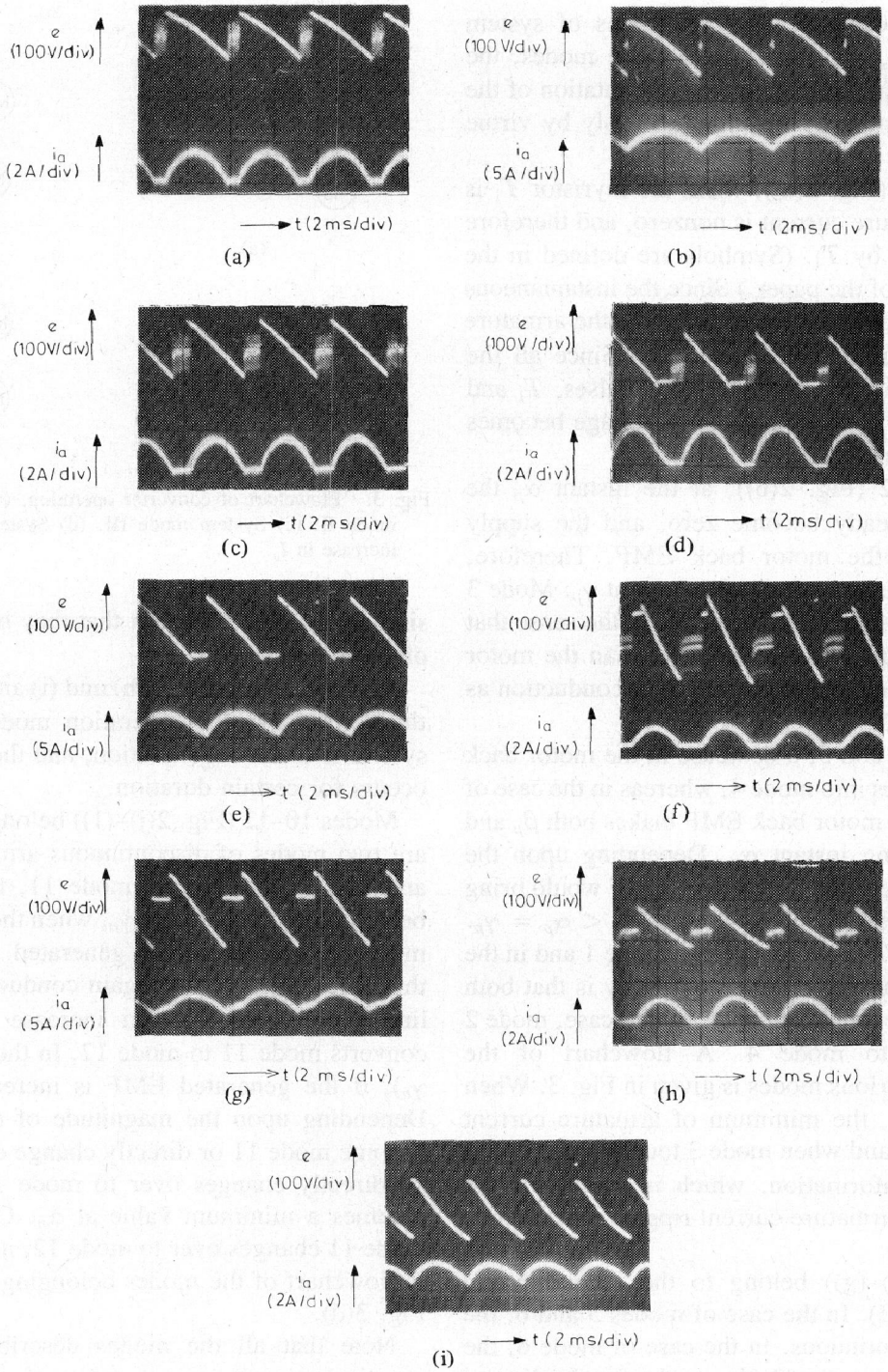

Fig. 4. Oscillograms of modes of converter operation. (a) Mode 3. (b) Mode 4. (c) Mode 5. (d) Mode 6. (e) Mode 7. (f) Mode 8. (g) Mode 9. (h) Mode 10. (i) Mode 12.

Authorized licensed use limited to: NATIONAL INSTITUTE OF TECHNOLOGY SURATHKAL. Downloaded on March 09,2021 at 06:21:29 UTC from IEEE Xplore. Restrictions apply.

III. Choice of Optimum Value of Filter Inductance

The armature current ripple is an important factor in dc drives since it adversely affects the machine commutation and causes derating of the motor. If the armature current is discontinuous, the motor speed regulation deteriorates and the sparking at the commutator brushes becomes more pronounced. Therefore, usually a filter inductance is incorporated in the armature circuit to limit the current ripple. On the other hand, the filter inductance cannot be made too large because of its cost, size, and weight considerations. The inevitable copper loss in the filter inductance, though small, is another factor which cannot be ignored. Therefore, it would be very useful to identify the optimum value of filter inductance required to eliminate discontinuous conduction in armature and to keep the current ripple within the specified permissible limits. Dubey [3] has suggested a method of choosing an optimum value of filter inductance for chopper-fed dc drives. This technique is extended here for three-phase fully controlled converter system. The equation governing the system performance can be written as (Fig. 1)

$$e = L_a \frac{di_a}{dt} + R_a i_a + E_b. \tag{1}$$

The voltages and the currents of the system are normalized against the following base values:

$$\text{base voltage} = \frac{3E_m}{\pi} \qquad \text{base current} = \frac{3E_m}{\pi R_a}.$$

Thus the normalized system performance equation is given by

$$e_n = \tan \psi \frac{di_{an}}{dwt} + i_{an} + E_{bn}. \tag{2}$$

To select an optimum value of filter inductance, the following curves must be obtained for a set of values of armature circuit time constant:

1) normalized maximum armature current ripple (MCR) versus the average output voltage;
2) normalized boundary curve separating the regions of continuous and discontinuous armature conduction on the speed–torque plane.

The analytical approach to obtaining these curves for a three-phase converter system with controlled flywheeling is briefly described. A computer flowchart is given in Fig. 5(a).

A. Calculation of MCR

For a particular firing angle, so far as the armature current is discontinuous, the current ripple depends upon the motor back EMF. When the armature current is continuous, any change in the motor back EMF causes change only in the dc component of armature current, and therefore, the ripple is independent of motor back EMF. Thus, for a particular firing angle, the armature current ripple becomes maximum and remains constant when the current is continuous.

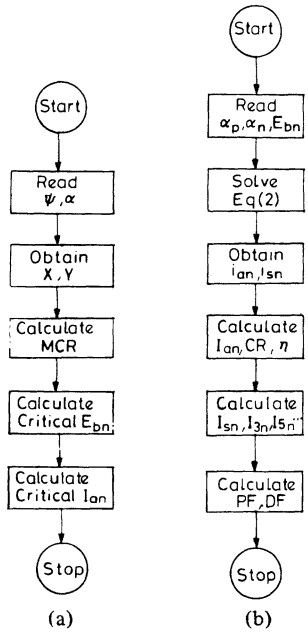

Fig. 5. Flowchart for system analysis.

MCR can be analytically calculated by obtaining current ripple for the continuous current modes of converter operation. The expression for armature current is obtained by solving (2), from which the expression for current slope can be derived. The instants at which the minimum and maximum of i_{an} occur (i.e., angles X and Y) can be determined by solving the expression for current slope. The MCR is then calculated with the help of the following expression:

$$\text{MCR} = \frac{i_{an\ \max} - i_{an\ \min}}{2}. \tag{3}$$

Four modes of converter operation exist (modes 4, 7, 9, and 12) in which the armature current is continuous. The expression for armature current for the various continuous current modes are given later. The expressions for the slopes can be derived from these expressions. Since the converter output voltage and current waveforms repeat after every $\pi/3$ rad, the solution of (2) is provided only for the interval $0 < wt < \pi/3$ in each case.

Mode 4: For the interval $0 < wt < \alpha_p$,

$$i_{an} = \cos\psi \left[\sin\left(\alpha_p + \frac{2\pi}{3} - \psi\right) + \left[\sin\left(\alpha_p + \frac{2\pi}{3} - \psi\right) - \sin\left(\alpha_p + \frac{\pi}{3} - \psi\right) \right] \cdot \exp\left\{ -\left(wt + \frac{\pi}{3} - \alpha_p \right) \cot\psi \right\} \div \left[1 - \exp\left(-\frac{\pi}{3} \cot\psi \right) \right] \right] - E_{bn}. \tag{4}$$

Authorized licensed use limited to: NATIONAL INSTITUTE OF TECHNOLOGY SURATHKAL. Downloaded on March 09,2021 at 06:21:29 UTC from IEEE Xplore. Restrictions apply.

For the interval $\alpha_p < wt < \pi/3$,

$$i_{an} = \cos\psi\left[\sin\left(wt+\frac{\pi}{3}-\psi\right) - \left[\sin\left(\alpha_p+\frac{\pi}{3}-\psi\right) - \sin\left(\alpha_p+\frac{\pi}{3}-\psi\right)\right] \cdot \exp\left[-(wt-\alpha_p)\cot\psi\right] \div \left[1-\exp\left(-\frac{\pi}{3}\cot\psi\right)\right] - E_{bn}. \quad (5)$$

Since there are two expressions for i_{an} in different intervals, it is useful to know the interval in which X and Y occur. Since, for continuous armature current, the instants X and Y are independent of average armature current, the interval in which they occur depends upon which of the discontinuous current modes comes in contact with the continuous current mode at the critical point (i.e., when the armature current is just continuous). In the present case, from Fig. 3(a), $\alpha_p \leqslant X$. In any case, $\alpha_p < Y$. Therefore, it is enough if the expression for current slope in the interval $\alpha_p < wt < \pi/3$ is obtained by differentiating (5).

Mode 7: In this case, $\pi/3 < \alpha_p < 2\pi/3$. For the interval $0 < wt < (\alpha_p - (\pi/3))$,

$$i_{an} = \cos\psi\left[\left[\sin\psi - \sin\left(\alpha_p+\frac{\pi}{3}-\psi\right) \cdot \exp\left\{-\left(\frac{2\pi}{3}-\alpha_p\right)\cot\psi\right\}\right] \cdot \exp(-wt\cot\psi) \div \left[1-\exp\left(-\frac{\pi}{3}\cot\psi\right)\right]\right] - E_{bn}. \quad (6)$$

For the interval $(\alpha_p - (\pi/3)) < wt < \pi/3$,

$$i_{an} = \cos\psi\left[\sin\left(wt+\frac{2\pi}{3}-\psi\right) - \left[\sin\left(\alpha_p+\frac{\pi}{3}-\psi\right) \cdot \exp\left\{-\left(\frac{\pi}{3}-\alpha_p\right)\cot\psi\right\} - \sin\psi\right]\exp(-wt\cot\psi) \div \left[1-\exp\left(-\frac{\pi}{3}\cot\psi\right)\right]\right] - E_{bn}. \quad (7)$$

In this case, both X and Y can be obtained (Fig. 3(b)) by differentiating (7) valid for the interval $(\alpha_p - (\pi/3)) < wt < \pi/3$.

Mode 9: For the internal $0 < wt < \alpha_n$,

$$i_{an} = -\cos\psi\left[\sin(wt-\psi) + \left[\sin\psi + \sin(\alpha_n-\psi) \cdot \exp\left\{-\left(\frac{\pi}{3}-\alpha_n\right)\cot\psi\right\}\right] \cdot \exp(-wt\cot\psi) \div \left[1-\exp\left(-\frac{\pi}{3}\cot\psi\right)\right]\right] - E_{bn}$$

For the interval $\alpha_n < \omega t < \pi/3$,

$$i_{an} = -\cos\psi\left[\left[\sin(\alpha_n-\psi)\exp\{-(wt-\alpha_n)\cot\psi\} + \sin\psi\exp(-wt\cot\psi)\right] \div \left[1-\exp\left(-\frac{\pi}{3}\cot\psi\right)\right]\right] - E_{bn}. \quad (9)$$

In this case, $X = \alpha_n$ and $0 < Y < \alpha_n$. Therefore, the expression for current slope is obtained by differentiating (8).

Mode 12: For the interval $0 < wt < (\alpha_n - (\pi/3))$,

$$i_{an} = -\cos\psi\left[\sin\left(wt+\frac{\pi}{3}-\psi\right) - \left[\sin\left(\alpha_n-\frac{\pi}{3}-\psi\right) - \sin(\alpha_n-\psi)\right] \cdot \exp\left\{-\left(wt+\frac{2\pi}{3}-\alpha_n\right)\cot\psi\right\} \div \left[1-\exp\left(-\frac{\pi}{3}\cot\psi\right)\right]\right] - E_{bn}. \quad (10)$$

For the interval $(\alpha_n - (\pi/3)) < wt < \pi/3$,

$$i_{an} = -\cos\psi\left[\sin(wt-\psi) - \left[\sin\left(\alpha_n-\frac{\pi}{3}-\psi\right) - \sin(\alpha_n-\psi)\right] \cdot \exp\left\{-\left(wt+\frac{\pi}{3}-\alpha_n\right)\cot\psi\right\} \div \left[1-\exp\left(-\frac{\pi}{3}\cot\psi\right)\right]\right] - E_{bn}. \quad (11)$$

From Fig. 3(d), $X \leqslant \alpha_n$. In any case, $Y < \alpha_n$. The expression for current slope is obtained by differentiating.

Fig. 6(a) shows the plot of MCR against the average output voltage. For the controlled flywheeling technique, the MCR assumes a peak value at $E_{on} = 0.4$ and reduces to zero with the average output voltage, whereas for the normal control technique, the peak MCR occurs at zero output voltage. These peak values of MCR are plotted against armature circuit time constant in Fig. 6(b).

B. Separation of Regions of Continuous and Discontinuous Armature Conduction

In order to separate the regions of continuous and discontinuous armature conduction in the speed–torque plane, it is required to obtain the critical values of motor back EMF (E_{bn}) and average armature current (I_{an}), at which the current is just continuous. Having obtained the angle at which i_{an} becomes minimum, in the earlier section, the critical E_{bn} can be obtained by forcing $i_{an}(X) = 0$ in the appropriate equations. The critical I_{an} can then be calculated by averaging the armature current for the particular value of critical back EMF. The expression for the critical values of I_{an} for various continuous current modes are

$$\text{mode 4: } I_{an(\text{critical})} = \cos\alpha_p - E_{bn(\text{critical})} \quad (12)$$

Authorized licensed use limited to: NATIONAL INSTITUTE OF TECHNOLOGY SURATHKAL. Downloaded on March 09,2021 at 06:21:29 UTC from IEEE Xplore. Restrictions apply.

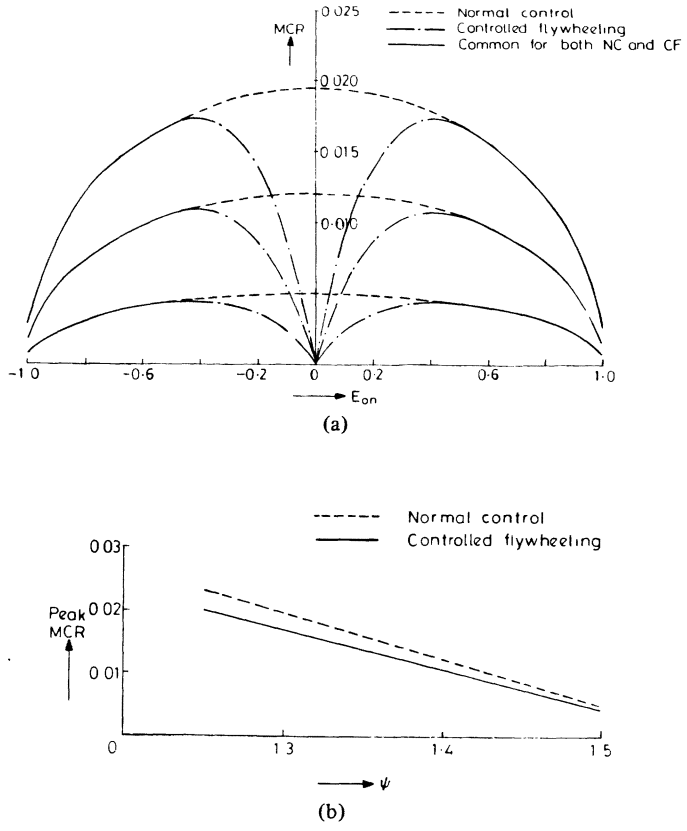

Fig. 6. (a) Normalized maximum armature current ripple. (b) Peak MCR verses armature time constant.

$$\text{mode 7: } I_{an(\text{critical})} = 1 + \cos\left(\alpha_p + \frac{\pi}{3}\right) - E_{bn(\text{critical})} \quad (13)$$

$$\text{mode 9: } I_{an(\text{critical})} = -(1 - \cos\ \alpha_n) - E_{bn(\text{critical})} \quad (14)$$

$$\text{mode 12: } I_{an(\text{critical})} = \cos\left(\frac{\pi}{3} + \alpha_n\right) - E_{bn(\text{critical})}. \quad (15)$$

Fig. 7 shows the normalized boundary curves separating the regions of continuous and discontinuous armature conduction for the controlled flywheeling and the normal control techniques. The armature current is continuous to the right of the boundary curve.

With the help of these boundary curves and the MCR characteristics, a filter inductance can be chosen such that the armature current remains continuous and the current ripple is kept below the specified permissible limits for worst-case load conditions.

From the knowledge of load on the motor shaft, a normalized contour of minimum torque for the whole range of motor speed is obtained and superposed over the boundary curves of Fig. 7. A filter inductance is so chosen that the boundary curve corresponding to the modified armature circuit time constant falls to the left of the minimum load contour. The value of filter inductance required to keep the MCR within the specified permissible limit is obtained from Fig. 6. The higher of the two values is finally chosen as the optimum filter inductance.

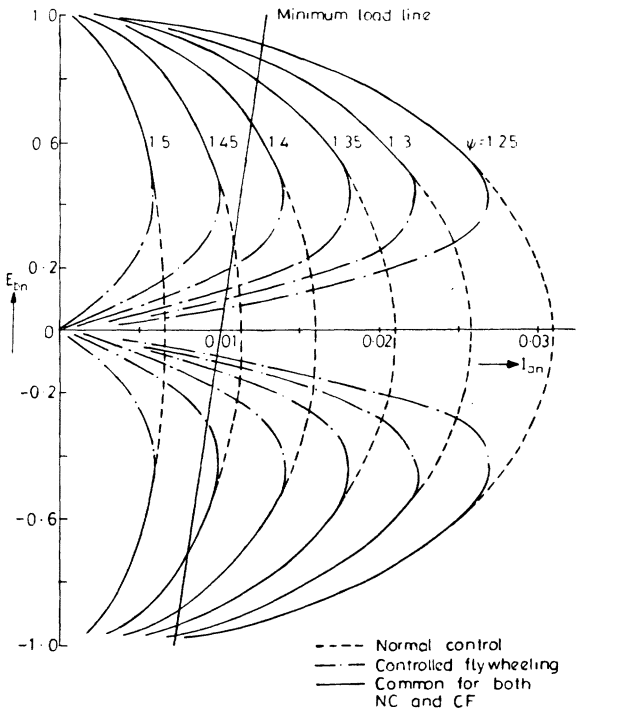

Fig. 7. Boundary curves separating regions of continuous and discontinuous armature conduction.

IV. System Analysis

The system is analyzed by simulating it in a digital computer. For any particular firing angle, the waveforms of converter output voltage, armature current, and source current are obtained from which the various parameters of system performance, such as motor speed–torque characteristics, armature current ripple, system efficiency, input power factor, distortion factor, source current harmonics, and source current (rms) are calculated. A computer flowchart for the purpose is given in Fig. 5(b). The formulas used for calculating the different parameters are

$$\text{armature current ripple} = \text{CR} = \frac{i_{an\max} - i_{an\min}}{2} \quad (16)$$

$$\text{overall power factor} = \text{PF} = \frac{\frac{3}{\pi}\int_0^{\pi/3} e_n i_{an}\, dwt}{\frac{\pi}{\sqrt{6}} I_{sn}} \quad (17)$$

$$\text{source current distortion factor} = \text{DF} = \frac{I_{1n}}{I_{sn}}. \quad (18)$$

The system efficiency is defined separately for motoring and regeneration conditions:

$$\text{motoring efficiency} = \eta_M = \frac{\text{power developed by the motor}}{\text{power input to the system}} = \frac{E_{bn} I_{an}}{\frac{3}{\pi}\int_0^{\pi/3} e_n i_{an}\, dwt} \quad (19)$$

Authorized licensed use limited to: NATIONAL INSTITUTE OF TECHNOLOGY SURATHKAL. Downloaded on March 09,2021 at 06:21:29 UTC from IEEE Xplore. Restrictions apply.

regeneration efficiency $= \eta_R$

$$= \frac{\text{power delivered to the source}}{\text{power generated by the motor}} = \frac{\frac{3}{\pi}\int_0^{\pi/3} e_n i_{an}\, dwt}{E_{bn} I_{an}}. \quad (20)$$

V. System Performance and Experimental Verification

The system performance is investigated on a 2.2-kW dc motor (Table III) load. Normalized speed-torque characteristics are obtained by plotting E_{bn} against I_{an} (Fig. 8). Since the range of firing angle for controlled flywheeling and normal control are different, the speed-torque characteristics are drawn for constant values of E_{on}. All the other system parameters, such as armature current ripple, system efficiency, power factor, source current distortion factor, source current harmonics, and rms value of source current are plotted against I_{an} for constant values of E_{bn} (Figs. 8–12). The fact that E_{bn} is held constant in plotting these curves facilitates the comparison of the two control techniques for the same developed power.

The speed-torque characteristics and system efficiency curves are experimentally verified, and these results are indicated by (o) in the corresponding diagrams. From the system performance curves, the following points are noted.

1) The armature current ripple is substantially lower for controlled flywheeling technique at low motor speeds (Fig. 9), which improves the machine commutation and reduces the derating of a motor.

2) Because of reduction in the armature current ripple, the system efficiency improves with controlled flywheeling technique at low motor speeds (Fig. 10).

3) Controlled flywheeling causes significant improvement in the overall system power factor (Fig. 11).

4) The drawback of controlled flywheeling technique is that it increases the harmonic content in the source current which is reflected in the reduction of source current distortion factor (Fig. 11).

5) The experimental results of motor speed-torque characteristics (Fig. 8) and system efficiency (Fig. 10) corroborate reasonably well with the theoretical results in the first quadrant but show a deviation in the fourth quadrant. This deviation is attributed mainly to the demagnetizing effect of armature reaction and partly to the device and brush contact resistances. These effects oppose each other in the first quadrant, which accounts for the close relationship between the predicted and experimental results, whereas in the fourth quadrant they aid each other and hence the notable deviation between the experimental and analytical results.

VI. Conclusion

The modes of operation of the three-phase fully controlled converter employing controlled flywheeling are identified, and their oscillograms are presented. The system is analyzed using a digital simulation technique, and a complete study of system

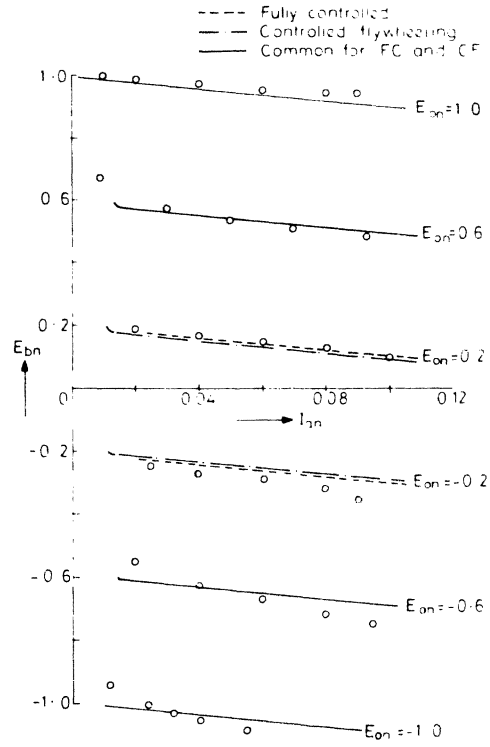

Fig. 8. Normalized speed-torque characteristics.

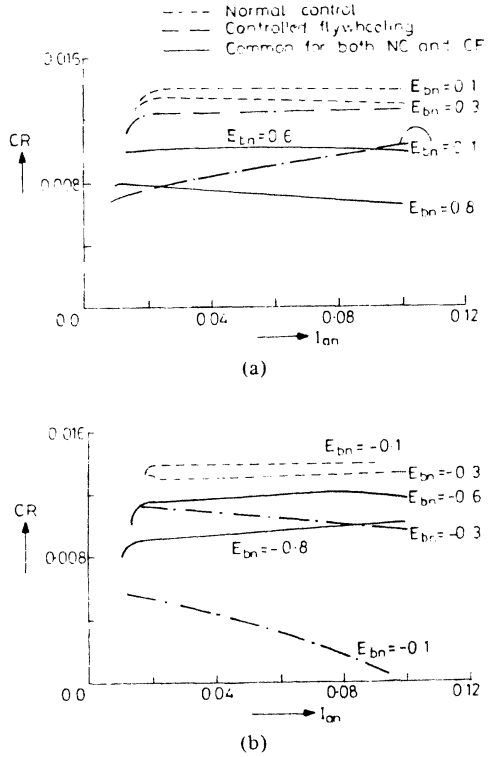

(a) (b)

Fig. 9. Normalized armature current ripple. (a) Motoring. (b) Regenerating.

Authorized licensed use limited to: NATIONAL INSTITUTE OF TECHNOLOGY SURATHKAL. Downloaded on March 09,2021 at 06:21:29 UTC from IEEE Xplore. Restrictions apply.

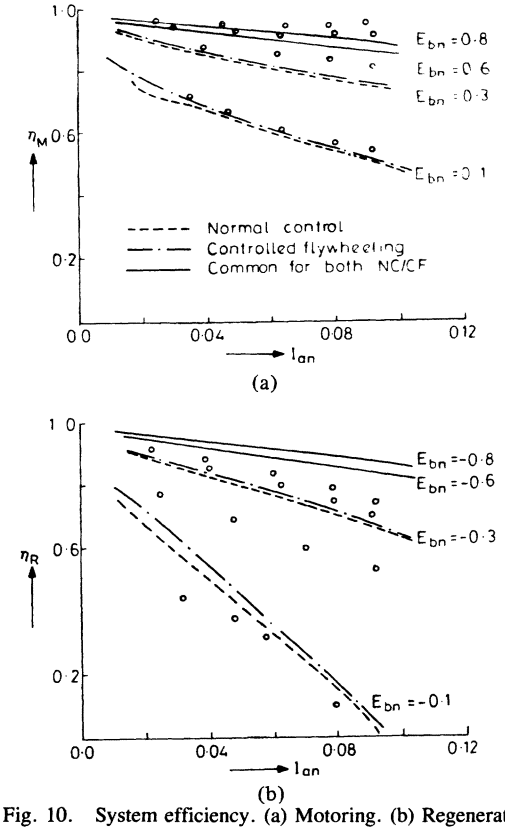

Fig. 10. System efficiency. (a) Motoring. (b) Regenerating.

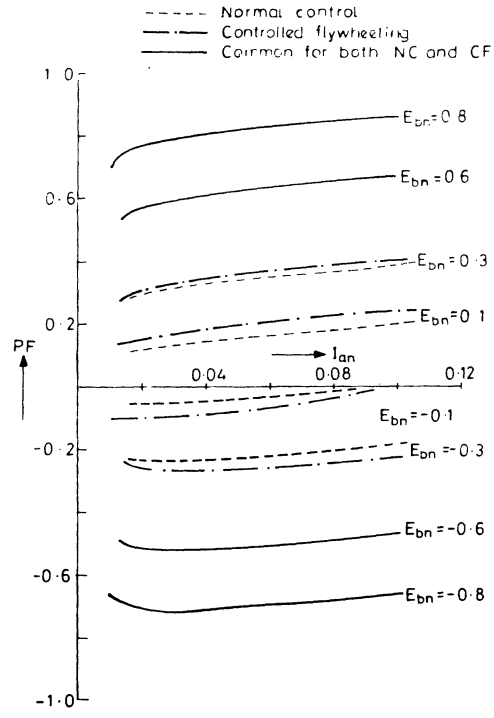

Fig. 11. Overall power factor.

performance is made. The theoretical results are compared with that of the normal control technique for the same developed shaft power.

An analytical approach is presented to obtain normalized nomograms for maximum armature current ripple and boundary curves separating the continuous and discontinuous arma-

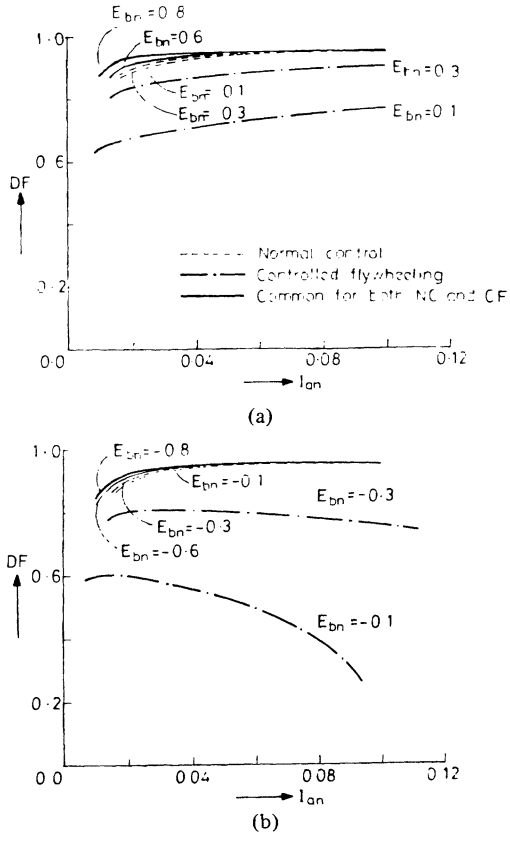

Fig. 12. Source current distortion factor. (a) Motoring. (b) Regenerating.

ture conduction in the speed–torque plane. With the help of these nomograms, an optimum value of filter inductance can be chosen for any motor.

As compared to normal control, controlled flywheeling offers a reduced zone of discontinuous conduction, lower armature current ripple, and higher system efficiency and power factor. These beneficial effects are obtained without any increase in the number or rating of the power circuit component and, therefore, without any significant increase in the cost of the drive. Larger harmonic content in the source current and complexity of firing circuit are the drawbacks of controlled flywheeling.

VII. Nomenclature

e, E_o	Instantaneous and average output voltage of converter, V.
E_b	Motor back EMF, V.
E_m	Peak supply voltage, V.
e_n, E_{on}, E_{bn}	Normalized values of e, E_o, and E_b.
i_a, I_a	Instantaneous and average armature current, A.
i_{an}, I_{an}	Normalized values of i_a and I_a.
MCR	Maximum normalized armature current ripple for a particular firing angle.
X	Angle at which i_a is minimum, rad.
Y	Angle at which i_a is maximum, rad.
α_p, α_n	Converter firing and flywheeling angles, rad.
β_p, β_n	Extinction angles, rad.
γ_p	$= \sin^{-1}(E_b/E_m) - (\pi/3)$, rad.
γ_n	$= \pi + \sin^{-1}(E_b/E_m)$, rad.

Authorized licensed use limited to: NATIONAL INSTITUTE OF TECHNOLOGY SURATHKAL. Downloaded on March 09,2021 at 06:21:29 UTC from IEEE Xplore. Restrictions apply.

ψ $= \tan^{-1}(wL_a/R_a)$, rad.
w Supply frequency, rad/s.

References

[1] W. Farrer and D. F. Andrew, "Fully controlled regenerative bridges with half controlled characteristics," *Proc. Inst. Elec. Eng.*, vol. 125, pp. 109–112, Feb. 1978.
[2] W. Drury, W. Farrer, and B. L. Jones, "Performance of thyristor bridge converters employing flywheeling," *Proc. Inst. Elec. Eng.*, Part B, vol. 127, pp. 268–276, July 1980.
[3] G. K. Dubey, "Calculation of filter inductance for chopper fed dc separately excited motor," *Proc. IEEE*, vol. 66, pp. 1671–1673, Dec. 1978.

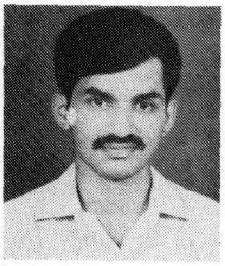

Subbanna P. Bhat received the B.E. degree in electronics and telecommunications and the M. Tech. degree in industrial electronics from the University of Mysore, India, and the Ph.D. degree from the Indian Institute of Technology, Kanpur, in 1974, 1977, and 1984, respectively.

He joined the faculty of the Department of Electrical Engineering, Karnataka Regional Engineering College, Surathkal, India, affiliated with the Mangalore University.

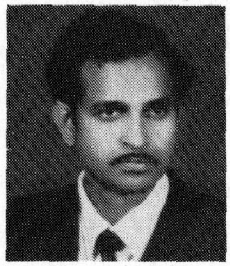

Gopal K. Dubey (SM'83) received the B.E. (Honors) degree from Jabalpur University, India in 1963, and the M. Tech degree in electrical drives and control and the Ph.D. degree in electrical drives from Indian Institute of Technology, Bombay, in 1965 and 1972, respectively.

He was a teacher trainee from 1963 to 1966, Lecturer from 1966 and 1972, and Assistant Professor from 1973 to 1977 in the Department of Electrical Engineering, Indian Institute of Technology, Bombay. He has been Professor in the Department of Electrical Engineering, Indian Institute of Technology, Kanpur, India, since 1978. He was a Visiting Research Fellow and Commonwealth Scholar in the Postgraduate School of Electrical and Electronic Engineering, University of Bradford, England, from October 1974 to December 1975. He was a Visiting Professor in the University of British Columbia, Vancouver, BC, Canada from August 1983 to August 1984, and in the Virginia Polytechnic Institute and State University, Blacksburg, VA, from September 1984 to June 1985. His fields of interest are electrical drives, power electronics, control systems, and engineering education. He is a coauthor (with S. R. Doradla, A. Joshi, and R. M. K. Sinha) of *Thyristorized Power Controllers* (Wiley Eastern) and authored over 100 research papers.

Dr. Dubey is a Fellow of the Institution of Engineers, India (1978). He was awarded Pandit Madan Mohan Malviya Memorial Gold Medal for 1975–1976 and the Institution Prize for 1977–1978 by the Institution of Engineers.

Authorized licensed use limited to: NATIONAL INSTITUTE OF TECHNOLOGY SURATHKAL. Downloaded on March 09,2021 at 06:21:29 UTC from IEEE Xplore. Restrictions apply.